25. H. J. Melosh, *Proc. Lunar Sci. Conf.* **9**, 3513 (1978); S. C. Solomon and J. W. Head, *Rev. Geophys.* **18**, 107 (1980); R. J. Willemann and D. L. Turcotte, *Proc. Lunar Planet. Sci.* **12B**, 837 (1981).

26. M. A. Wieczorek and R. J. Phillips, *J. Geophys. Res.* **103**, 1715 (1998).

27. A. B. Kucinskas and D. L. Turcotte, *Icarus* **112**, 104 (1994); A. B. Kucinskas, D. L. Turcotte, J. Arkani-Hamed, *J. Geophys. Res.* **101**, 4725 (1996). For Fig. 1, we used a density of 2.8 g/cm^3 for the crust and 3.3 g/cm^3 for the mantle.

28. The LLR sun/(Earth + moon) mass ratio is 328900.559 ± 0.002, which gives in TDB (Barycentric Dynamical Time) units GM(Earth + moon) = 403503.236 ± 0.002 km^3/s^2. The artificial satellite result is GM(Earth) = 398,600.4356 ± 0.0008 km^3/s^2

in TDB units [J. C. Ries, R. J. Eanes, C. K. Shum, M. M. Watkins, *Geophys. Res. Lett.* **19**, 529 (1992)].

29. J. O. Dickey *et al.*, *Science* **265**, 482 (1994).

30. J. G. Williams, X. X. Newhall, J. O. Dickey, *Planet. Space Sci.* **44**, 1077 (1996).

31. B. G. Bills, *J. Geophys. Res.* **100**, 26297 (1995).

32. L. L. Hood and J. H. Jones, *ibid.* **92**, 396 (1987).

33. S. Mueller, G. J. Taylor, R. J. Phillips, *ibid.* **93**, 6338 (1988).

34. A. B. Binder, *ibid.* **85**, 4872 (1980).

35. For example, see H. E. Newsom, in *Origin of the Moon*, W. K. Hartmann, R. J. Phillips, G. J. Taylor, Eds. (Lunar and Planetary Institute, Houston, TX, 1986), pp. 203–230.

36. A. G. W. Cameron, *Icarus* **126**, 126 (1997); R. M. Canup and L. W. Esposito, *ibid.* **119**, 427 (1996).

37. A. G. W. Cameron and R. M. Canup, paper presented at 29th Lunar and Planetary Science Conference, Lunar and Planetary Institute, Houston, TX, 16 to 20 March 1998.

38. We thank G. Neumann and M. Zuber for providing the latest lunar topography solutions from Clementine and F. Lemoine for his lunar gravity field and spacecraft model information for processing the Clementine tracking data. Helpful discussions with D. Turcotte are appreciated. LLR solutions were done with the help of D. H. Boggs, and LP data were processed with the help of E. Carranza, D. N. Yuan, and N. Rappaport. The research was carried out by the Jet Propulsion Laboratory, California Institute of Technology, under a contract with NASA.

Lunar Surface Magnetic Fields and Their Interaction with the Solar Wind: Results from Lunar Prospector

R. P. Lin, D. L. Mitchell,* D. W. Curtis, K. A. Anderson, C. W. Carlson, J. McFadden, M. H. Acuña, L. L. Hood, A. Binder

The magnetometer and electron reflectometer experiment on the Lunar Prospector spacecraft has obtained maps of lunar crustal magnetic fields and observed the interaction between the solar wind and regions of strong crustal magnetic fields at high selenographic latitude (30°S to 80°S) and low (∼100 kilometers) altitude. Electron reflection maps of the regions antipodal to the Imbrium and Serenitatis impact basins, extending to 80°S latitude, show that crustal magnetic fields fill most of the antipodal zones of those basins. This finding provides further evidence for the hypothesis that basin-forming impacts result in magnetization of the lunar crust at their antipodes. The crustal magnetic fields of the Imbrium antipode region are strong enough to deflect the solar wind and form a miniature (100 to several hundred kilometers across) magnetosphere, magnetosheath, and bow shock system.

The primary objective of the magnetometer and electron reflectometer (MAG/ER) experiment on Lunar Prospector (LP) is to investigate the nature and origin of the moon's magnetic fields. Measurements by early lunar orbiting spacecraft showed that the moon has no global dipole magnetic field (*1*). The discovery of strong stable components of natural remanent magnetization in many of the returned lunar samples (*2*) and the detection of surface magnetic fields of up to hundreds of nanoteslas at the landing sites (*3*) were thus major surprises of the Apollo program. Paleointensity measurements on the returned samples suggest that the lunar surface field was comparable in intensity to the present-day terrestrial surface field from about 3.6 to 3.8 billion years ago (Ga) and about an order of magnitude lower before and after this time period (*4*).

The Apollo 15 and 16 subsatellite magnetometers in low, 100-km-altitude orbits detected regions of crustal magnetic fields of 100-km scale size (*5*), and electron reflection (ER) magnetometry revealed hundreds of magnetic patches on the surface, ranging in size from ≲7 km, the resolution limit of the observations, to ∼500 km (*6*). In general, the lunar highlands have stronger fields than the younger maria (*5*, *6*), and there is evidence that some of the far-side basin ejecta are magnetized (*7*). The largest concentrations of surface magnetic fields in the ∼20% of the moon sampled by the subsatellites are located within zones centered on the antipodes of the Imbrium, Serenitatis, Crisium, and Orientale

impact basins (*8*). These four large circular ringed basins have ages between ∼3.85 and 3.6 Ga (*9*), about the same as the most strongly magnetized returned samples. With the exception of a linear magnetic feature that follows the Rima Sirsalis rille (*10*) and a tendency for strong anomalies to occur in association with unusual albedo markings of the Reiner Gamma class (*11*), however, no clear-cut association of surface magnetic fields with surface selenological features was found. Furthermore, the directions of the crustal fields of the >100-km-size regions, as determined by the subsatellite magnetometers, appear to be randomly distributed (*12*). A MAG/ER experiment flown on Mars Global Surveyor recently discovered similar localized patches of surface magnetic fields at Mars, but with surface field strengths ∼1000 times as strong (*13*).

The MAG/ER on LP, which is based on instruments flown on Mars Observer (*14*) and Mars Global Surveyor, is designed to map surface magnetic fields with high sensitivity (∼0.01 nT at the surface) and spatial resolution (∼4 km) over the entire moon (*15*). The MAG measures the vector magnetic field at the spacecraft, and when the external field is steady and plasma disturbances (which can be detected by the ER) are minimal, the lunar crust magnetic field intensity and direction at the spacecraft altitude can be determined by subtracting the external field.

ER magnetometry (*6*) depends on the magnetic mirror effect, that is, the reflection of charged particles from regions of increased magnetic fields. In a uniform field the particles move along helical paths of constant pitch angle (α, the angle between the particle velocity and the magnetic field direction) and radius (called the gyro-radius). However, if the field strength increases in the direction of motion as the surface is approached, particles with pitch angles greater than a cutoff pitch angle (α_c) will be reflected back along the lines of force, whereas those with pitch angle below α_c will impact the surface and be lost. The cutoff pitch angle depends on the ratio of the total field strength at the surface to that at the spacecraft. A technique for identifying

R. P. Lin, Space Sciences Laboratory and Physics Department, University of California, Berkeley, CA 94720, USA. D. L. Mitchell, D. W. Curtis, K. A. Anderson, C. W. Carlson, J. McFadden, Space Sciences Laboratory, University of California, Berkeley, CA 94720, USA. M. H. Acuña, NASA Goddard Space Flight Center, Greenbelt, MD 20771, USA. L. L. Hood, Lunar and Planetary Laboratory, University of Arizona, Tucson, AZ 85721, USA. A. Binder, Lunar Research Institute, Gilroy, CA 95020, USA.

*To whom correspondence should be addressed. E-mail: mitchell@ssl.berkeley.edu

lunar surface magnetic fields consists of measuring the electron reflection coefficient, R, which is the ratio of the electron flux reflected back from the surface ($90° < \alpha < 180°$) to the incoming flux ($0° < \alpha < 90°$) (16). The region sampled is located about at the intersection of the extrapolation of the magnetic field vector with the surface, and the spatial resolution is set by the particle gyro-diameter. Electrons from a few electron volts (eV) to tens of kiloelectron volts energy, which are always present in the lunar environment, are ideal for this application because they have small gyro-diameter ($\sim$1 to 100 km) and travel at high speed.

Crustal magnetic fields. A map of the 220-eV reflection coefficient shows the distribution of magnetic fields in the lunar crust (Fig. 1). The observed reflection coefficients correspond to surface field strengths that are mostly in the $\sim$1 to 5 nT range; the highest reflectivity (0.78) implies a field strength of $\sim$10 nT. This reflectivity map covers a region of the lunar far side containing the antipodal zones of the Imbrium and Serenitatis impact basins, where some of the strongest crustal magnetic fields were observed previously from orbit. The Apollo 15 and 16 subsatellites were in near-equatorial orbits, and hence the previous ER measurements sampled only a fraction of these two basin antipodes: down to $\sim$35°S latitude for Imbrium and $\sim$30°S for Serenitatis. The LP map shows that strong surface fields nearly fill the inner Imbrium antipodal ring, but are shifted northward by $\sim$5° and perhaps westward by a few degrees. Substantial variations in field strength are evident within the Imbrium antipodal ring; for example, maxima are located at $\sim$20°S, 170°E, $\sim$43°S, 170°E, and possibly $\sim$36°S, 175°E. Strong surface fields are also found to extend to the southern edge of the Serenitatis basin antipode, filling most of the antipode except the area east of $\sim$205°E longitude. The spur extending to the southeast appears to be a separate nearby region. Two slightly weaker magnetic regions are seen at high southern latitudes, centered at $\sim$58°S, 175°E and $\sim$55°S, 188°E, roughly antipodal to Mare Frigoris.

The correspondence of surface magnetic fields with the antipodal zones strengthens the hypothesis that the crustal magnetization is associated with the formation of young large-impact basins. The hypervelocity ($>$10 km/s) impacts that form such large basins will produce a plasma cloud that expands around the moon in about 5 min, compressing and amplifying the preexisting ambient magnetic field at the antipode (17). The amplified field should remain for $\sim$1 day before the cloud becomes too tenuous. This is shorter than the cooling time for large masses of rock, so thermoremanent magnetization is unlikely. However, shock remanent magneti-

zation (SRM) associated with the focusing of seismic energy at the antipode (18) and with basin ejecta impacting in the antipode region may occur. Basin ejecta should arrive at the antipode within tens of minutes after the impact, and peak shock pressures from their impact are calculated to exceed 10 GPa (19), sufficient for acquisition of SRM (20). The association of strong surface fields with the antipodes of these young impact basins suggests that the ambient fields were enhanced between 3.85 and 3.6 Ga. This is consistent with the paleomagnetic data from the returned samples, which imply relatively steady $\sim$10^{-5} to 10^{-4} T ambient fields around the moon in that epoch. Such strong fields are unlikely to be of solar or terrestrial origin (21); a field of lunar origin, perhaps from a core dynamo, appears more feasible.

Direct measurements of the crustal fields at spacecraft altitude by the LP magnetometer can provide directional information. Reliable separation of the surface and external fields can generally only be performed in the geomagnetic tail lobes, where the ambient field is steady. Mapping of crustal fields with this technique, which requires many passes through the tail lobes, is in progress. One especially strong anomaly with a radial component of about -3 nT at 88-km altitude has been detected at 23°S and 123°W (nearly antipodal to the Crisium impact basin). It is probably identical to one detected previously with Apollo subsatellite magnetometer data (11, 22) and ER data (6). The Crisium antipodal region is marked by swirl-like albedo markings (11), which may result from magnetic deflection of the solar wind and, hence, depletion of implanted solar wind hydrogen in the uppermost soil layers (23). This hypothesis implicitly assumes that implanted hydrogen is a necessary component of the process that results in optical darkening of the lunar surface.

Solar wind interaction. Because the moon has a low electrical conductivity ($\sigma <$ 10^{-4} ohm/m) to depths of $\sim$200 km (24) and has only a weak global magnetic field if any at all (1), the solar wind normally flows virtually unimpeded to the surface where it is absorbed (25). The solar wind magnetic field passes through the moon with only a slight inductive interaction with the more electrically conducting interior (26) and reemerges into the plasma void of the solar wind wake. The system of currents that result from formation of the plasma void slightly amplifies the magnetic field within the wake and depresses the field at the wake boundary (27).

Occasionally, a sharply peaked enhancement of the solar wind magnetic field was observed just outside the wake. At distances of $\sim$1000 to 7000 km downstream from the solar wind terminator plane (defined as the plane including the moon's center and per-

pendicular to the solar wind flow direction), these enhancements were typically 25% of the ambient field and were observed to flare away from the moon (28). At the 100-km altitudes of the Apollo subsatellites, enhancements by factors of 2 to 3 were observed, located at an angle of up to $\sim$10° in front of the solar wind terminator (29). A variety of mechanisms have been proposed to explain these magnetic field amplifications: (i) interaction of the solar wind with a tenuous lunar atmosphere (30); (ii) induction of magnetic fields in electrically isolated "conducting islands" near the surface (31); and (iii) deflection of the solar wind by patches of strong crustal magnetic fields (32). Although the physical details of the magnetic field amplifications are not yet fully understood, Explor-
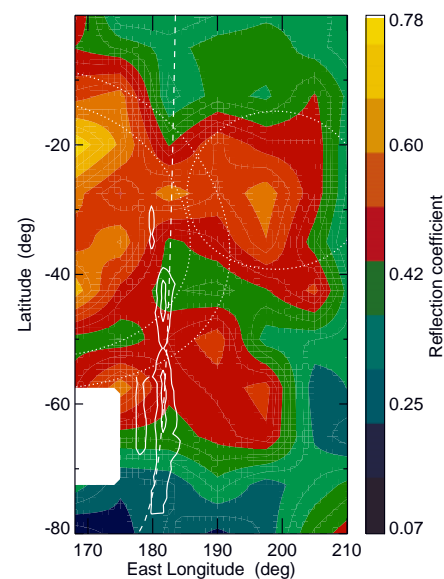
Fig. 1. The electron reflection coefficient, a measure of crustal magnetic fields (16), is mapped over a region of the lunar far side in a cylindrical equidistant projection. These data were obtained during the first four passes (February to May 1998) through the geomagnetic tail (but outside of the current sheet), where the magnetic field and electron flux are steady. Reflection coefficients from >1000 three-dimensional samples, each with a spatial resolution of $\sim$4 km, are averaged into 7.5° by 7.5° bins ($\sim$200 km on a side); then smooth contours are drawn around the binned data and color coded. The antipodal zones of the Imbrium and Serenitatis ringed impact basins are indicated by the dotted circles. The two circles for Imbrium correspond to its main rim $\sim$1200 km in diameter and a partial rim at 1500 km (9). For Serenitatis the single rim is $\sim$740 km in diameter. The solid contours show where the spacecraft (at an altitude of $\sim$100 km) passed through large amplifications of the solar wind magnetic field that form as the solar wind is shocked and deflected by the crustal magnetic field. The contours are at 20 and 27 nT, and the ambient field is nearly constant at $\sim$10 nT. The orbit track corresponding to the second enhancement in Fig. 2 is shown by the dashed line.

er 35 and Apollo subsatellite observations established that the enhancements occur only when specific regions of the crust are near the solar wind terminator (*29*, *32*), the same regions that were later found to possess strong magnetic fields by Apollo subsatellite magnetometer and ER mapping.

Perturbation of the solar wind by these magnetized regions will give rise to magnetohydrodynamic (MHD) waves, which have typical velocities of $v_m \sim 40$ to 80 km/s in the solar wind. In the moon's frame, these waves are carried downstream at the solar wind velocity of $v_{sw} \sim 400$ km/s, so the MHD wave front forms a Mach cone that flares out at an angle of $\tan^{-1}(v_m/v_{sw})$ with respect to the solar wind flow direction. The magnetic field enhancements were observed to be accompanied by similar enhancements in the plasma density (*33*), but there was no clear observational evidence for a shock. Therefore, these effects could have been produced either by "limb shocks" or merely MHD wave "limb compressions."

When the moon is in the solar wind, the most prominent feature of the LP electron measurements is the plasma void, where the flux of 40-eV electrons drops by nearly three orders of magnitude (Fig. 2). Low-energy electrons that might travel along the magnetic field into the wake are excluded by an electrostatic potential that forms at the wake boundary to prevent the buildup of charge. Strong, sharply peaked enhancements (factors of 2 to 3) of the magnetic field amplitude are observed outside of the plasma void on four of the five orbits shown as the LP spacecraft passes over the same general region of the lunar surface. These enhancements are not seen upstream by the WIND spacecraft and therefore must originate from the moon.

The magnetic field direction remains nearly the same as that of the unperturbed solar wind field. The small rotation is consistent with the solar wind field being compressed and draped around an obstacle located northwest (upstream) of the spacecraft. No enhancement is detected during the fourth orbit (~23:10), when the solar wind dynamic pressure more than doubles (Fig. 2). This behavior is expected if strong surface magnetic fields are deflecting the solar wind, forming a small magnetosphere. As the solar wind pressure is increased, the surface fields are further compressed and amplified until they are overwhelmed and the solar wind directly impacts the surface. Enhanced surface fields have been detected by magnetometers at the Apollo landing sites at times when the solar wind dynamic pressure increased (*34*).

The enhancements peak at latitudes ranging from 32°S to 66°S (Fig. 1), where the solar wind flow direction makes angles of $\chi \sim 45°$ to $66°$ to the local surface normal. (The
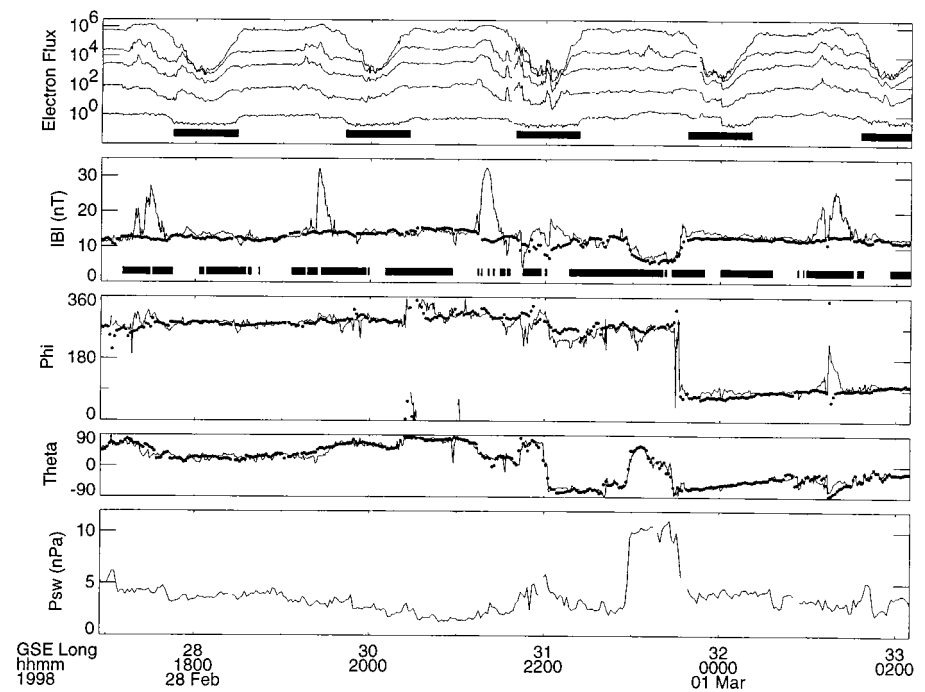
Fig. 2. Time series of electron and magnetic field measurements obtained when the moon was in the solar wind. The series spans five consecutive orbits passing over selenographic longitudes near 0° and 180°; successive orbits are separated by ~1° in longitude at the equator. Electron flux (cm^{-2} s^{-1} sr^{-1} eV^{-1}) is shown at five energies (top to bottom): 40, 140, 340, 800, and 2950 eV. Solid bars below the 2950-eV trace indicate times when the spacecraft was in the moon's optical shadow. The magnetic field amplitude and direction in selenocentric solar ecliptic coordinates are shown as solid lines in the next three panels. Measurements of the solar wind magnetic field by the WIND spacecraft, located ~1.2 million km upstream of the moon, are time-shifted to allow for the ~50-min solar wind travel time from WIND to LP and superimposed as solid dots over the LP observations. Solid bars below the magnetic field amplitude indicate times when LP is magnetically connected to the lunar surface. (Bottom) The solar wind dynamic pressure ($P_{sw} = \rho v^2$, where ρ and v are the solar wind mass density and flow velocity, respectively) as measured by WIND and time-shifted to LP's position. The moon's geocentric solar ecliptic (GSE) longitude is indicated along the time axis.

angle to the solar wind terminator plane is given by $90° - \chi$.) The peak of the field enhancement is located at angles of ~24° to 45° in front of the solar wind terminator plane, compared with only ~10° for the strongest compressions observed by the Apollo subsatellites (*35*). MHD waves originating from anywhere on the moon's surface cannot travel fast enough against the solar wind flow to reach the spacecraft at ~100-km altitude and 24° ahead of the solar wind terminator plane. Thus, the magnetic enhancements at LP's position imply the presence of a shock wave.

The second enhancement of Fig. 2 occurred at a time when the solar wind magnetic field was relatively stable. High time resolution observations of this enhancement (Fig. 3) begin with the LP spacecraft at 45°N latitude, traveling at ~100-km altitude toward the south pole (Fig. 1). Initially, the spacecraft is on magnetic field lines that do not intersect the moon and therefore represent the unperturbed solar wind. The plasma and magnetic field are steady in this region (Fig. 3). As the spacecraft passes into the southern

hemisphere, the magnetic field begins to connect to the lunar surface. At these times, fluctuations in the electron fluxes appear, including short bursts in the 140- and 340-eV energy channels.

As LP reaches 29°S (time B in Fig. 3), the electron fluxes abruptly increase and their energy distribution changes (Fig. 4), indicating that electrons are energized and not simply compressed. This is accompanied by a 20% increase in the magnetic field strength and the appearance of magnetic turbulence, including whistler mode wave activity at ~2.5 Hz. Similar wave activity is observed in all four of the enhancements (Fig. 2). Whistlers are commonly observed at and upstream from Earth's bow shock (*36*), but the electron energization provides the most direct evidence for the presence of a shock wave.

Intense electron and magnetic field turbulence persists up to the large magnetic ramp just before LP reaches 59°S (time C in Fig. 3). The magnetic field rotates by ~20° at the ramp, which is consistent with draping of the field and deflection of the solar wind around an obstacle located to the north and west
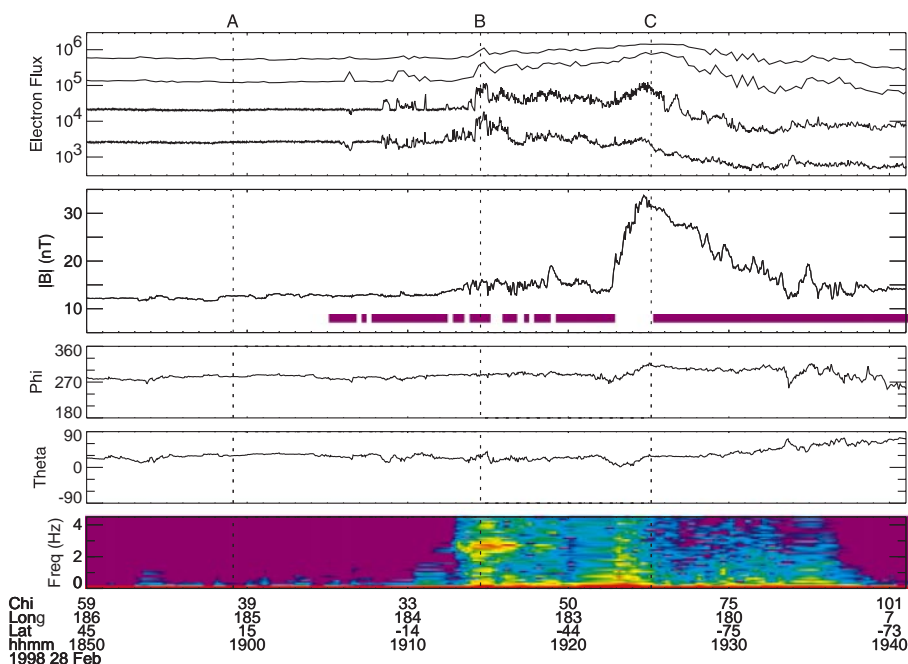
Fig. 3. High-resolution time series of electron and magnetic field measurements spanning part of the second orbit shown in Fig. 2. Notation is the same as in Fig. 2, except that the electron energies are 40, 60, 140, and 340 eV (top to bottom). (Bottom) The spectral density obtained by Fourier transforming the magnetic field amplitude. The logarithmic color scale ranges from 5×10^{-6} (violet) to 5×10^{-3} (red) nT^2/Hz. Vertical dashed lines indicate times when LP is in the undisturbed solar wind (A), crossing the shock wave surface (B), and near the peak magnetic amplification (C). The moon-centered selenographic coordinates of the spacecraft (Long, Lat) and the angle that the solar wind flow direction makes with the local surface normal (Chi) are indicated along the time axis.

Fig. 4. Electron spectra (flux in $cm^{-2} s^{-1} sr^{-1} eV^{-1}$ versus energy) at the times indicated in Fig. 3. Solid circles on spectrum A show the center energies of each channel.

Fig. 5. Schematic of the solar wind interaction with a crustal magnetic field near the edge of the Imbrium antipodal zone. The crustal field is represented by a dipole, which is at the focus of a hyperbolic shock wave surface that intersects the spacecraft (solid dot) and is symmetric about a line parallel to the solar wind flow direction (bold arrow). The moon's outline and the spacecraft altitude are drawn to scale. The extent of the Imbrium antipodal zone is shown by the solid trace just inside the moon's outline. The directions of the magnetic field (B) before and after the shock crossing are based on measurements shown in Fig. 3. By analogy with Earth's magnetosheath, the field lines inside the shock wave surface are assumed to drape around the dipole.
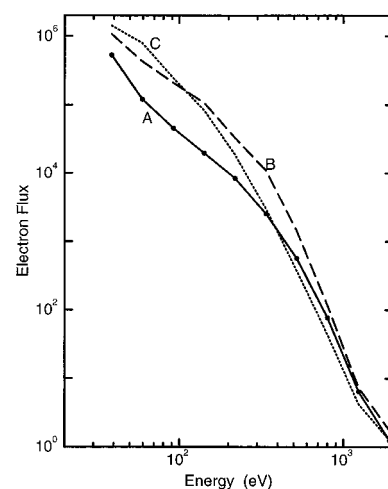
(toward the Imbrium antipode). There is an apparent separation between the onset of electron energization and the main magnetic ramp that probably results from the spacecraft trajectory relative to the shock wave surface: Between 29°S and 59°S the spacecraft is probably traveling nearly tangent to the shock wave and only crosses the magnetic ramp when the shock wave flares out to meet the spacecraft.

The inferred shock geometry is shown schematically in Fig. 5. We assume a single dipole located near the edge of the Imbrium antipode and a hyperbolic shock wave surface centered on the dipole and symmetric about a line parallel to the solar wind flow direction. As the spacecraft moves closer to the magnetic obstacle, the inferred shock wave surface dips below the orbital altitude, a geometry that is suggested by the time profile of the enhancement (Fig. 3) and the location of the orbit track relative to regions of strong surface magnetic fields (Fig. 1). Because the surface magnetic fields within the Imbrium antipodal ring appear patchy at the 200-km resolution of Fig. 1 and even more structure may be present on smaller scales, the actual shock wave surface could be rather complicated. However, because LP observes the shock wave some distance downstream and away from the antipode, the surface fields immediately upstream from the spacecraft
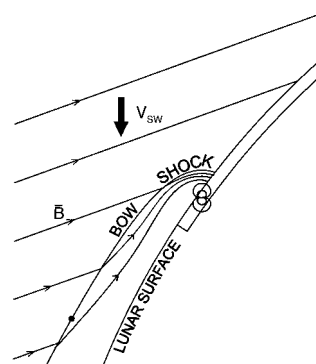
probably dominate the observed signature.

Variations in the anomaly profile from orbit to orbit depend on many parameters in addition to the strength and topology of the surface field, such as the solar wind dynamic pressure (Fig. 2), the angle that the solar wind flow makes with the surface, and the orientation of the solar wind magnetic field. The measured signature further depends on the trajectory of the spacecraft through the anomaly. Analysis of many anomalies and complete mapping of the surface magnetic fields will be necessary to unravel the details of this interaction.

The presence of a shock wave implies that at least some of the surface magnetic fields within the Imbrium antipodal zone are sufficiently strong to stand off the solar wind, that is, to exclude the solar wind from a volume around the crustal field. A lower limit to the required surface field strength can be estimated by balancing the component of the solar wind dynamic pressure normal to the surface with the magnetic pressure provided by the crustal field: $\mathbf{B}^2/4\mu_0 = P_{sw} \cos^2\chi$, where χ is the angle between the solar wind velocity and the surface normal. For $P_{sw} \sim 3$ nPa and $\chi \sim 60°$ (Figs. 2 and 3), this expression yields a crustal field strength of ~40 nT. Surface field strengths in excess of 100 nT were measured at the Apollo 14 and 16 landing sites (3), but in order to deflect the solar wind, the field

must also be coherent over horizontal scales much larger than the proton gyro-radius (~30 km in a 12-nT field). Whenever the crustal magnetic field stands off the solar wind, it effectively forms a miniature magnetosphere—the smallest known in the solar system.

References and Notes

1. Upper limit of $\sim 2 \times 10^{-8}$ of Earth's dipole moment [C. T. Russell *et al.*, *Proc. Lunar Planet. Sci. Conf.* **5**, 2747 (1978)].
2. Reviewed in M. Fuller and S. Cisowski, in *Geomag-*

netism, J. Jacobs, Ed. (Academic Press, Orlando, FL, 1987), vol. 2, p. 306.

3. Reviewed in P. Dyal *et al.*, *Rev. Geophys. Space Phys.* **12**, 568 (1974).

4. S. M. Cisowski *et al.*, *J. Geophys. Res. Suppl.* **88**, A691 (1983).

5. P. J. Coleman *et al.*, *Proc. Lunar Planet. Sci. Conf.* **3**, 2271 (1972).

6. K. A. Anderson *et al.*, *Space Sci. Instrum.* **1**, 439 (1975). R. P. Lin, *Phys. Earth Planet. Int.* **20**, 271 (1979).

7. K. A. Anderson and D. E. Wilhelms, *Earth Planet. Sci. Lett.* **46**, 107 (1979).

8. R. P. Lin, K. A. Anderson, L. L. Hood, *Icarus* **74**, 529 (1988).

9. D. E. Wilhelms, in *Geology of the Terrestrial Planets*, NASA SP–469 (NASA, Washington, DC, 1984), p. 107.

10. K. A. Anderson *et al.*, *Earth Planet. Sci. Lett.* **34**, 141 (1977).

11. L. L. Hood, P. J. Coleman, Jr., D. E. Wilhelms, *Science*, **205**, 53 (1979).

12. There is some evidence that the virtual geomagnetic poles of these regions (the direction of the magnetic south pole of the moon-centered dipole that accounts for the observed crustal magnetic field) cluster around three axes. Changes in the global dipole orientation may have been caused by dynamo field reversals and reorientation of the moon's spin axis by giant impacts, although this interpretation is controversial [S. K. Runcorn, *Proc. Lunar Planet. Sci. Conf.* **11**, 1867 (1980); *Phys. Earth Planet. Int.* **29**, 135 (1982); L. L. Hood, *Proc. Lunar Planet. Sci. Conf.* **12**, 817 (1981)].

13. M. H. Acuña *et al.*, *Science* **279**, 1676 (1998).

14. M. H. Acuña *et al.*, *J. Geophys. Res.* **97**, 7799 (1992).

15. The ER and experiment electronics are mounted on a 2.5-m boom that was deployed shortly after launch. The MAG sensor, which is separated from the ER electronics by a 1.2-m deployable boom, is a wide-range (up to 65,536 nT), low-noise (6 pT root mean square), high-sensitivity (as low as 2 pT) triaxial fluxgate magnetometer that measures magnetic fields from dc up to a sample rate of 18 Hz. The ER sensor consists of a symmetric hemispherical electrostatic analyzer that focuses incoming electrons onto an imaging detector that provides fine ($\sim 1.4°$) angular resolution in the plane of its 360° by 14° disk-shaped field of view (FOV). The analyzer is stepped in voltage through the entire energy range (~ 10 to 20 keV) 32 times per spacecraft spin, and the ER is oriented so that its FOV covers the full sky (4π sr) every half spin (~ 2.5 s). Thus, the full three-dimensional distribution of electrons can be obtained every half spin, but because of telemetry rate limitations it is only transmitted once every 16 spins (80 s, corresponding to ~ 120 km of spacecraft motion). High temporal or spatial resolution mapping (2.5 s or ~ 4 km) is provided in two energy channels by computing pitch angle bins with the magnetic field direction measured by the MAG, sorting the electron counts into the bins on board the spacecraft, and sending only the one-dimensional pitch angle distribution to the ground.

16. If the field varies spatially and the fractional change in the field is small over the distance traveled by the electron in one gyration, then the adiabatic approximation holds: $(\sin^2\alpha)/|\mathbf{B}|$ = constant. For an isotropic pitch angle distribution, R depends only on the solid angle subtended by α_c, and we obtain $|\mathbf{B}_s|$ = $|\mathbf{B}_h|/(1 - R^2)$, where $|\mathbf{B}_s|$ and $|\mathbf{B}_h|$ are the magnetic field strengths at the surface and the spacecraft, respectively. Hence, R provides a monotonic but non-linear measure of the surface field strength, which is the vector sum of $\mathbf{B}_h$ and the crustal remanent field, $\mathbf{B}_r$. Coulomb scattering at the surface generates a small background of upward traveling electrons, resulting in $R \sim 0.05$ even in the absence of magnetic reflections. Surface magnetic fields a few times stronger than the field measured at the spacecraft can increase the reflection coefficient to nearly unity. For typical field strengths at the moon's location in the geomagnetic tail, R is a useful measure of crustal magnetic fields in the ~ 0.1 to 10 nT range. The dynamic range of ER magnetometry can be extended

to $\sim 10^{-2}$ to 10^4 nT by measuring α_c directly from the pitch angle distribution.

17. L. Hood and Z. Huang, *J. Geophys. Res.* **96**, 9837 (1991).

18. Hilly terrain antipodal to the Imbrium and Orientale basins is thought to be produced by the focusing of seismic waves generated by those impacts [P. H. Schultz and D. E. Gault, *Moon* **12**, 159 (1975)].

19. L. L. Hood and A. Vickery, *J. Geophys. Res.* **89**, C211 (1984).

20. M. Fuller *et al.*, *Moon* **9**, 57 (1974).

21. The early sun's magnetic field may have been several orders of magnitude stronger than the present-day field, but by ~ 4 Ga, its field was probably far too weak to account for $\sim 10^{-5}$-T fields at the Earth's orbital distance. Such strong fields are also incompatible with terrestrial paleomagnetic data. For a review, see R. T. Merrill, M. W. McElhinny, P. L. McFadden, in *The Magnetic Field of the Earth: Paleomagnetism, the Core, and the Deep Mantle*, R. Dmowska and J. R. Holton, Eds. (International Geophysics Series, Academic Press, San Diego, CA, 1996), vol. 63, pp. 217–247.

22. L. Hood *et al.*, *J. Geophys. Res.* (*Suppl.*) **92**, E396 (1981).

23. L. Hood and G. Schubert, *Science* **208**, 49 (1980).

24. P. Dyal *et al.*, *Proc. Lunar Planet. Sci. Conf.* **5**, 3059 (1974).

25. B. E. Goldstein, *J. Geophys. Res.* **79**, 23 (1974).

26. Reviewed in C. P. Sonett, *Rev. Geophys. Space Phys.* **20**, 411 (1982).

27. D. S. Colburn, R. G. Currie, J. D. Mihalov, C. P. Sonett, *Science* **158**, 1040 (1967); C. J. Owen *et al.*, *Geophys. Res. Lett.* **23**, 1263 (1996).

28. N. F. Ness *et al.*, *J. Geophys. Res.* **73**, 3421 (1968); D. S. Colburn *et al.*, *ibid.* **76**, 2940 (1971).

29. C. T. Russell and B. R. Lichtenstein, *ibid.* **80**, 4700 (1975).

30. G. L. Siscoe and N. R. Mukherjee, *ibid.* **77**, 6042 (1972).

31. J. V. Hollweg, *ibid.* **75**, 1209 (1970).

32. C. P. Sonett and J. D. Mihalov, *ibid.* **77**, 588 (1972).

33. G. L. Siscoe *et al.*, *ibid.* **74**, 59 (1969).

34. P. Dyal *et al.*, *Nature* **236**, 381 (1972); P. Dyal *et al.*, *Proc. Lunar Sci. Conf.* **4**, 2925 (1973).

35. Apollo-like compressions would peak near 78°S latitude in Fig. 1.

36. D. H. Fairfield, *J. Geophys. Res.* **79**, 1368 (1974); M. Hoppe and C. T. Russell, *Nature* **287**, 417 (1980).

37. The contributions of P. Turin, R. Ulrich, R. Sterling, and J. Scheifele to the development of the experiment and data processing system are gratefully acknowledged. D.L.M. acknowledges discussions with S. D. Bale. WIND data were obtained from the Solar Wind Experiment (K. W. Olgilvie) and Magnetic Fields Investigation (R. P. Lepping) key parameter files. Research at the University of California, Berkeley, was supported by NASA through subcontract LMSC-HG80E477OR from Lockheed-Martin.

Global Elemental Maps of the Moon: The Lunar Prospector Gamma-Ray Spectrometer

D. J. Lawrence*, W. C. Feldman, B. L. Barraclough, A. B. Binder, R. C. Elphic, S. Maurice, D. R. Thomsen

Lunar Prospector gamma-ray spectrometer spectra along with counting rate maps of thorium, potassium, and iron delineate large compositional variations over the lunar surface. Thorium and potassium are highly concentrated in and around the nearside western maria and less so in the South Pole–Aitken basin. Counting rate maps of iron gamma-rays show a surface iron distribution that is in general agreement with other measurements from Clementine and the Lunar Prospector neutron detectors.

The Lunar Prospector (LP) gamma-ray spectrometer (GRS) has acquired global maps of elemental composition of the moon. It has long been known that such maps will significantly improve our understanding of lunar formation and evolution (*1*). For example, one long-standing issue of lunar formation concerns the bulk composition of the moon. There are suggestions from Apollo, Galileo, and Clementine data that the moon is enriched in refractory elements (Al, U, and Th) and FeO compared to Earth (*2*). If so, then

---

D. J. Lawrence, W. C. Feldman, B. L. Barraclough, R. C. Elphic, D. R. Thomsen, Space and Atmospheric Sciences, Mail Stop D466, Los Alamos National Laboratory, Los Alamos, NM 87545, USA. Telephone: 505-667-0945, Fax: 505-665-7395, e-mail: djlawrence@lanl.gov. A. B. Binder, Lunar Research Institute, Gilroy, CA, 95020, USA. S. Maurice, Observatoire Midi-Pyrénées, Toulouse, France.

*To whom correspondence should be addressed.

lunar origin models that assume that most of the moon's material comes from Earth's mantle would not be correct. Another question is the compositional variability and evolution of the lunar highlands, which contain KREEP-rich materials [potassium (K), rare earth elements (REE), and phosphorus (P)]. KREEP-rich rocks are thought to have formed at the lunar crust-mantle boundary as the final product of the initial differentiation of the moon. The distribution of these rocks on the lunar surface therefore gives information about how the lunar crust has evolved over time. Other issues that can be addressed in the future using GRS data include: (i) identifying and delineating basaltic units in the maria; (ii) determining the composition of ancient or "cryptic" mare units found in the highlands using Clementine data (*3*), and searching for more of these units using mainly the Fe and Ti data; (iii) identifying and

Science

Lunar Surface Magnetic Fields and Their Interaction with the Solar Wind: Results from Lunar Prospector

R. P. Lin, D. L. Mitchell, D. W. Curtis, K. A. Anderson, C. W. Carlson, J. McFadden, M. H. Acuña, L. L. Hood and A. Binder

ARTICLE TOOLS	http://science.sciencemag.org/content/281/5382/1480
RELATED CONTENT	file:/contentpending:yes
REFERENCES	This article cites 30 articles, 3 of which you can access for free http://science.sciencemag.org/content/281/5382/1480#BIBL
PERMISSIONS	http://www.sciencemag.org/help/reprints-and-permissions